Spectral Unmixing using Machine Learning

A dissertation submitted in
partial fulfilment for the degree of

Master of Technology

in

Computer Science

by

Debashis Dhar
Roll no. - **CS2413**

under the supervision of

Dr. Sarbani Palit
Computer Vision and Pattern Recognition Unit (CVPRU)

Indian Statistical Institute, Kolkata
June, 2026

CERTIFICATE

This is to certify that the dissertation titled "Spectral Unmixing with Machine Learning" submitted by Debashis Dhar to the Indian Statistical Institute, Kolkata, fulfills the requirements for the degree of Master of Technology in Computer Science. The work presented in this dissertation is an authentic and original contribution conducted under my supervision and guidance. I confirm that this dissertation adheres to all the necessary academic standards and regulations of the institute.

Sarbani Palit

Dr. Sarbani Palit
CVPR Unit
Indian Statistical Institute
Kolkata - 700108
India

Acknowledgement

I would like to express my gratitude to Dr. Sarbani Palit, my advisor at the Computer Vision and Pattern Recognition Unit of the Indian Statistical Institute in Kolkata. Her expert guidance, unwavering support, and inspiring insights have been invaluable throughout my academic journey. Dr. Palit's extensive knowledge and innovative ideas have significantly contributed to my understanding of various topics and have been crucial in shaping my research skills and research aptitude.

I am very thankful to Subhranil Mustafi, Senior Research Fellow at the Indian Statistical Institute, for his essential assistance in acquiring the datasets, notes and necessary materials for this study. His continuous input of ideas and continuous support have played an important role in the successful completion of this project. After various discussion related to topic we came with some improvement in our work.

I also extend my gratitude to all the faculty members at the Indian Statistical Institute for their invaluable advice, insights, and teachings, which have provided a vital perspective to my research work.

I am thankful to all my friends for their ongoing assistance and motivation. My appreciation goes out to everyone who has contributed to my personal and academic growth, even if I have not explicitly mentioned them here.

Declaration

I, **Debashis Dhar**, with Roll No. **CS2413**, hereby declare that the material presented in the dissertation titled **Spectral Unmixing Using Machine Learning.** represents original work carried out by me for the degree of **Master of Technology in Computer Science** at the **Indian Statistical Institute, Kolkata**.

Furthermore, I affirm that no sections of this report have been sourced or copied from external references without proper attribution. I am aware that any instances of plagiarism or the use of unacknowledged materials from third parties will be treated with the utmost seriousness and consequences.

Debashis Dhar
M.Tech (CS), CS2413
Indian Statistical Institute

Abstract

Spectral Unmixing is an important field of study nowadays which focuses on generating fractional abundance of each pixel into constituent materials .In this thesis we have tried to unmix each pixel into three end members namely glacial lake,debris and others with primarily focusing on glacial lake.We have performed various methods of linear spectral unmixing and non linear spectral unmixing. These methods are applied on the collected LandSat Data of east Himalayan terrain .Experimental results demonstrate the effectiveness of the proposed approach in achieving high accuracy and efficiency in glacier lake tracking on LandSat data.

Keywords: Spectral Unmixing, Linear Mixing Model, Non-linear Spectral Unmixing, East Himalayan Terrain, Landsat, Glacial Lake Tracking.

Contents

List of Figures

List of Tables

Chapter 1

Introduction

1.1 Literature Survey

Mountain Glaciers are among the most sensitive indicator of climate change.They form new supra glacial lakes by variation in mass,changes in flow velocity .Later from these supraglcaial lakes pro glacial lakes might be formed. These dynamic changes make the glaciar accountable of the climate change.Though these are studied for understanding climate change mainly but these lakes are also source of fresh water sustaining the life of billions of people downstream.Glacial meltwater also supports domestic use ,hydropower generation.If due to the climate change accelerated ice loss happens then it threatens not only mountain ecosystems and also the socio economic stability of vast downstream regions based on seasonal melt water. Thus with the growing vulnerability we observe an urgent need to accurately monitor them and we need to predict the glacier dynamics with the changing climate.

1.2 Our Proposed Work

In this thesis, we have studied a region of Eastern Himalayas. The region of interest (ROI) lies in the eastern Himalayan belt, covering parts of Arunachal Pradesh (India) and adjoining Himalayan terrain.The vertices listed on the map correspond to the four corner coordinates of a polygon, forming a quadrilateral that encloses a high-altitude mountainous region characterized by dense drainage networks, steep relief, and extensive cryospheric features. The visible labels on the map, such as the areas around Jigme Dorji National Park and nearby valleys, indicate that this region encompasses glaciated basins and alpine terrain. The ROI is defined by four corner coordinates in Degree–Minute–Second (DMS) format:

- $28^\circ\,12'\,45''$ N, $089^\circ\,43'\,46''$ E
- $28^\circ\,10'\,52''$ N, $090^\circ\,36'\,28''$ E

- $27^\circ\,51'\,04''$ N, $090^\circ\,33'\,59''$ E
- $27^\circ\,52'\,43''$ N, $089^\circ\,43'\,16''$ E

This places the study area within the eastern Himalaya ,encompassing glaciated catchments and high relieve terrain near protected mountain regions.This region contains the five end members a brief description of each one of them is given below

1. **Light Debris** Light debris corresponds to glacier surfaces covered by fine-grained, relatively reflective material such as sand, silt, and weathered rock fragments.
2. **Dark Debris** Dark debris represents coarse, rock-rich supraglacial material with low reflectance due to its high absorptivity and increased thermal response.
3. **Glacial Lake** This endmember captures both supraglacial and proglacial water bodies formed by meltwater accumulation.
4. **Cloud** Although not a surface feature, cloud cover is frequent in high-mountain remote sensing imagery and strongly influences observed spectra.
5. **Vegetation** Vegetation represents alpine forests, shrubs, and grasslands in the lower and mid-altitude zones surrounding the glaciers.

In this thesis the primary goal is to correctly generate fractional abundance of each pixel of the study area and derive the quantity of each end member in every pixel.

Chapter 2

Dataset

2.1 Study Area

In this thesis we have studied a region of Eastern Himalaya. The region of interest (ROI) lies in the eastern Himalayan belt, spanning parts of Arunachal Pradesh (India) and the adjoining Himalayan terrain. The vertices listed on the map correspond to the four corner coordinates of a polygon, forming a quadrilateral that encloses a high-altitude mountainous region characterized by dense drainage networks, steep relief, and extensive cryospheric features. The labels visible on the map, such as areas around Jigme Dorji National Park and nearby valleys. Its size and well-defined structure make it a key feature in the regional glaciological landscape.

Study Area (ROI)

Eastern Himalaya (Arunachal Pradesh and nearby regions of Jigme Dorji National Park)

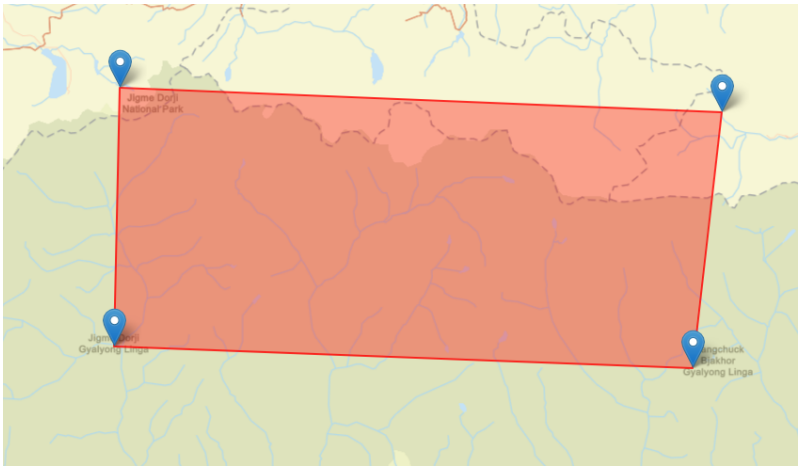

Figure 2.1: Region of high-altitude glacier-dominated terrain.

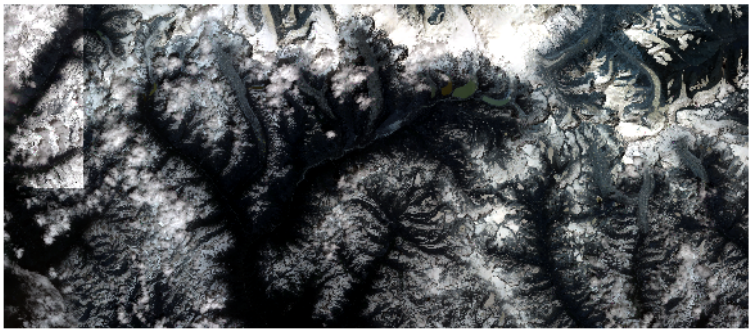

(a) PlanetScope Image used for validation

(b) Binary Mask

(c) LandSat Image used as input

Figure 2.2: PlanetScope image, generated occlusion mask, and corresponding input image used for spectral analysis.

Chapter 3

Reference Abundance Generation and Validation

3.0.1 Note on Endmember Representation

The abundance aggregation and validation experiment presented in this chapter was performed with five original endmember classes: Light Debris, Dark Debris, Vegetation, Cloud, and Glacial Lake. The objective of this validation was to assess the accuracy of the proposed geometric abundance generation and Planet-to-Landsat aggregation framework while preserving all physically identifiable surface materials.

For the subsequent spectral unmixing experiments, these five endmembers were merged into three classes. Light Debris and Dark Debris were merged to form a single *Debris* class , Vegetation and Cloud were combined into an *Others* class, the *Glacial Lake* class.

Consequently, the validation results reported in this chapter correspond to the original five-endmember representation, whereas all spectral unmixing models and comparative analyses presented in the subsequent chapters employ the final three-endmember formulation consisting of Debris, Others, and Glacial Lake.

3.1 Pure Geometric Fractional Abundance Estimation

Let the input raster image be defined over a spatial grid of size $H \times W$, and let there be C classes represented by polygonal regions (ROIs).

3.1.1 Abundance Definition

For each pixel (i, j) and class c, the fractional abundance can be defined as:

$$A_c(i,j) = \frac{\text{Area}\,(P_{ij} \cap R_c)}{\text{Area}\,(P_{ij})}$$

where:

- P_{ij} is the polygon corresponding to pixel (i, j)
- R_c is the region of interest for class c
- $A_c(i, j) \in [0, 1]$

3.1.2 Pixel Geometry Construction

Each pixel is converted into a polygon using the raster affine transform:

$$P_{ij} = \text{Box}(x_{ij} - \frac{\Delta x}{2},\ y_{ij} - \frac{\Delta y}{2},\ x_{ij} + \frac{\Delta x}{2},\ y_{ij} + \frac{\Delta y}{2})$$

where (x_{ij}, y_{ij}) is the pixel center and $\Delta x, \Delta y$ are pixel resolutions.

3.1.3 Algorithm

1. Load raster metadata (transform, CRS)
2. Load all the ROI shapefiles and make them to raster CRS
3. Assign each ROI a class index $c \in \{1, \ldots, C\}$
4. Dissolve polygons within each class
5. Initialize abundance tensor:

$$A \in \mathbb{R}^{C \times H \times W}$$

6. For each pixel (i, j):
   (a) Construct pixel polygon P_{ij}
   (b) Use spatial index to find intersecting ROIs
   (c) For each class c:

$$A_c(i,j) = \frac{\text{Area}(P_{ij} \cap R_c)}{\text{Area}(P_{ij})}$$

7. Save A as a multi-band raster

3.1.4 Properties

- $0 \leq A_c(i, j) \leq 1$
- $\sum_{c=1}^{C} A_c(i, j) \leq 1$

3.2 Aggregation from Planet to Landsat Resolution

Let $A_c^{(P)}(i,j)$ denote the fractional abundance at Planet resolution (3m), and $A_c^{(L)}(u,v)$ denote the abundance at Landsat resolution (30m).

3.2.1 Objective

The goal is to compute coarse-resolution abundance using an area-weighted aggregation of fine-resolution pixels.

3.2.2 Overlap Computation

For a Landsat pixel L_{uv} and a Planet pixel P_{ij}, the overlap along one dimension is defined as:

$$\text{overlap}(a,b) = \max\left(0, \min(a_{\max}, b_{\max}) - \max(a_{\min}, b_{\min})\right)$$

The 2D overlap area is:

$$\text{Area}_{ij} = \text{overlap}_x \times \text{overlap}_y$$

3.2.3 Aggregation Formula

The Landsat abundance is computed as:

$$A_c^{(L)}(u,v) = \frac{\sum\limits_{i,j} A_c^{(P)}(i,j) \cdot \text{Area}_{ij}}{\text{Area}(L_{uv})}$$

3.2.4 Algorithm

1. Reproject Planet data to Landsat CRS if required
2. For each Landsat pixel (u,v):
   (a) Determine spatial bounds of L_{uv}
   (b) Identify overlapping Planet pixels
   (c) Compute overlap areas Area_{ij}
   (d) Compute weighted sum:

$$A_c^{(L)}(u,v) = \frac{\sum A_c^{(P)}(i,j) \cdot \text{Area}_{ij}}{\text{Area}(L_{uv})}$$

3. Store output as multi-band raster

3.2.5 Properties

- $0 \leq A_c^{(L)}(u, v) \leq 1$
- $\sum_{c=1}^{C} A_c^{(L)}(u, v) \approx 1$

3.3 Validation of Planet-derived Abundance

The Planet-derived abundance aggregated to Landsat resolution is validated against the actual Landsat abundance.

3.3.1 Pixel-wise Comparison

For each valid pixel (u, v), we compare:

$$x = A_{\text{planet}}^{(L)}(u, v), \quad y = A_{\text{actual}}^{(L)}(u, v)$$

3.3.2 Evaluation Metrics

Coefficient of Determination (R^2)

$$R^2 = 1 - \frac{\sum (y - x)^2}{\sum (y - \bar{y})^2}$$

Root Mean Square Error (RMSE)

$$\text{RMSE} = \sqrt{\frac{1}{N} \sum (y - x)^2}$$

3.3.3 Results

The obtained results show strong agreement across all bands:

- R^2 values range from 0.83 to 0.93
- RMSE values are consistently low (< 0.05)

3.3.4 Discussion

- High R^2 and low RMSE indicate accurate geometric aggregation
- Residuals are centered around zero, indicating minimal bias

3.3.5 Conclusion

The results confirm that the proposed geometric method provides a physically consistent and accurate estimation of fractional abundance. Remaining discrepancies are primarily due to sensor and environmental factors rather than algorithmic limitations.

3.3.6 Quantitative Results

The validation results across all bands are summarized below:

Table 3.1: Per-Endmember Quantitative Evaluation Metrics

Endmember	R^2	**RMSE**
Light Debris	0.9291	0.0389
Dark Debris	0.8331	0.0404
Cloud	0.8473	0.0183
Vegetation	0.8313	0.0140
Glacial Lake	0.8994	0.0321

3.3.7 Discussion

The high R^2 values confirm that the geometric aggregation method preserves the underlying abundance relationships effectively.

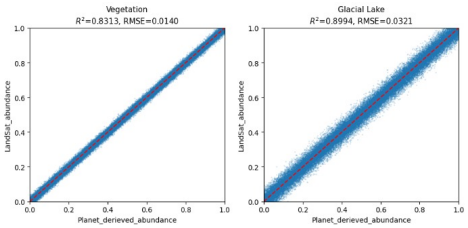

(a) R^2 Scatter Plot – light debris, dark debris and cloud

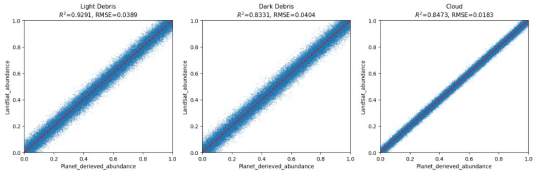

(b) R^2 Scatter Plot – for glacial lake and vegetation

Figure 3.1: Scatter plot comparison between predicted and ground-truth abundance values showing coefficient of determination (R^2) performance.

Chapter 4

Endmember Aggregation Strategy

The original scene contained five extracted endmember classes, namely Light Debris, Dark Debris, Vegetation, Cloud, and Glacial Lake. Although the endmember extraction process identified these five spectrally distinct surface components, the abundance estimation experiments were ultimately performed using three aggregated classes: Debris, Others, and Glacial Lake.

The aggregation process was motivated by both spectral similarity analysis and semantic interpretation of the identified endmembers. To quantitatively evaluate spectral separability, Spectral Angle Distance (SAD) analysis was performed among all extracted endmember classes.

Spectral Angle Distance Map

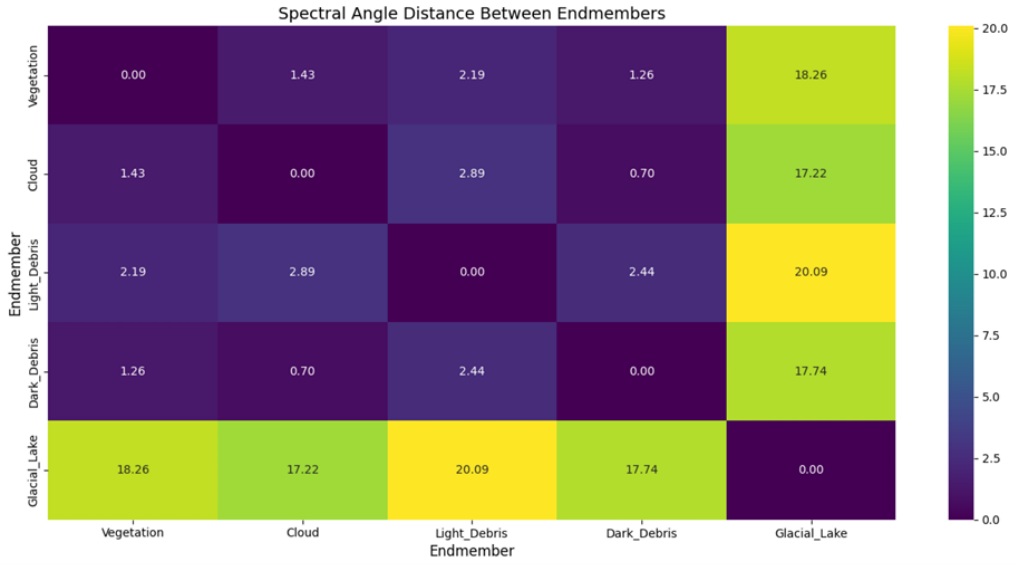

Figure 4.1: Pairwise spectral angle distance among the extracted endmember classes.

4.1 Spectral Separability Analysis

Spectral Angle Distance (SAD) was employed to evaluate the spectral separability among the extracted endmember classes. For each endmember class, a representative mean spectral signature was computed by averaging the spectral responses of all pixels belonging to that class.

Let

$$\boldsymbol{\mu}_c = [\mu_{c,1}, \mu_{c,2}, \ldots, \mu_{c,B}]^T$$

denote the mean spectral signature of class c, where B represents the number of spectral bands. The mean spectrum is calculated as

$$\boldsymbol{\mu}_c = \frac{1}{N_c} \sum_{i=1}^{N_c} \mathbf{x}_i,$$

where N_c denotes the total number of pixels belonging to class c, and $\mathbf{x}_i$ represents the spectral vector of the i^{th} pixel.

The spectral angle between two endmember classes p and q was then computed as

$$\text{SAD}(p, q) = \cos^{-1}\left(\frac{\boldsymbol{\mu}_p^T \boldsymbol{\mu}_q}{\|\boldsymbol{\mu}_p\| \, \|\boldsymbol{\mu}_q\|}\right),$$

where $\boldsymbol{\mu}_p^T \boldsymbol{\mu}_q$ denotes the dot product between the two mean spectral vectors, and $\|\boldsymbol{\mu}_p\|$ and $\|\boldsymbol{\mu}_q\|$ represent their Euclidean norms. Pairwise SAD values were calculated for all combinations of endmember classes to construct a spectral separability matrix. Smaller SAD values indicate greater spectral similarity between classes, whereas larger values correspond to increased spectral discrimination.

The resulting SAD matrix indicates that the Glacial Lake endmember exhibits substantially larger spectral angles relative to the remaining endmembers, demonstrating strong spectral separability. In contrast, Light Debris, Dark Debris, Vegetation, and Cloud exhibit comparatively smaller spectral angle distances among themselves.

4.2 Semantic Interpretation of Endmembers

Although spectral similarity provides a quantitative basis for aggregation, the final grouping was not determined solely from the SAD matrix. The physical meaning and environmental significance of each endmember had been considered.

The Light Debris and Dark Debris classes originate from the same underlying

rock-derived debris materials commonly found on glacier surfaces. The primary difference between these classes is their reflectance and absorption characteristics. Since both classes represent debris-covered glacier surfaces, combining them into a single *Debris* category is both spectrally and semantically justified.

The Vegetation and Cloud endmembers were aggregated into a common category termed *Others*. The Himalayan glacier region investigated in this study contains only limited alpine vegetation, while the selected satellite imagery was acquired under conditions of minimal cloud coverage.

4.3 Final Aggregation Scheme

Based on the combined evidence from spectral separability analysis and semantic interpretation, the five extracted endmember classes were aggregated into three final categories for abundance estimation:

- **Debris**: Light Debris + Dark Debris
- **Others**: Vegetation + Cloud
- **Glacial Lake**: Retained as an independent class

Chapter 5

Methodology

5.1 Preparation of Satellite Datasets

Landsat Imagery

Landsat data has a very low spectral resolution of 30m * 30m. We have collected this data with almost negligible cloud cover and applied all unmixing algorithm on this data.

Planet Imagery

Planet satellite image had very high spatial resolution .One single cell of the picture of the planet satellite used to be 3m * 3m .Hence it was used for validation in our task.

5.2 Data Preprocessing

5.2.1 Radiometric and Atmospheric Correction

All of the collected images were converted to surface reflectance values by atmospheric correction.

5.2.2 Cloud and Shadow Masking

Those datasets were selected for which cloud cover was zero and the shadow were minimal .Thus we have the cloud and shadow masked .

5.3 Region of Interest (ROI) Selection

ROI has various reference imageries and we have collected five shapefiles for each of the classes like vegetation, dark debri ,light debri,glacial lake and cloud.Based on all these ROI we had the initial endmembers but later they were merged as mentioned in the previous chapter.

5.4 Linear Spectral Unmixing

5.4.1 Motivation for Linear Modeling

Linear spectral unmixing is based on the assumption that the observed spectral response of a pixel can be represented as a weighted linear combination of the spectral signatures of its constituent endmembers. This assumption is appropriate when the materials within a pixel contribute independently to the recorded reflectance and multiple scattering effects are negligible.

5.4.2 Linear Mixing Model

Linear Mixing model assumes that the reflectance value of each pixel is the linear combination of the all endmember spectrum and hence we can write the reflectance value of each pixel as summation of the different values of each pixels. Thus we have the linear mixing model.

5.4.3 Abundance Estimation

While generating the fractional abundance we have the fact that the sum of all the fractions sum up to unity and each of the fraction of the endmember is greater than equal to zero.

5.5 Non-Linear Spectral Unmixing

5.5.1 Motivation for Non-Linear Modeling

Non-linear spectral unmixing is required to capture complex surface interactions.Although the linear mixing model provides a simple and physically interpretable framework, it may not adequately represent the complex interactions present in real-world glacier environments. In mountainous regions, multiple scattering effects, terrain-induced illumination variations, shadowing, and interactions among neighboring surface materials can lead to nonlinear spectral mixing.

5.5.2 Autoencoder-Based Unmixing Framework

For spectral consistency it is necessary that the original and reconstructed spectra should be as close as possible that is the real spectra and the reconstructed spectra must be as close as possible .Hence we have the autoencoder based unmixing framework. We have used an regularied loss function .

5.5.3 Graph Attention CNN-Based Unmixing Framework

In hyperspectral and multispectral unmixing, neighboring pixels often exhibit strong spatial and spectral correlations. Traditional pixel-wise reconstruction approaches fail to effectively capture these contextual dependencies.

Initially, convolutional neural networks are utilized to extract local spatial-spectral representations from the input image. These features show texture, edge, and material distribution information. Subsequently, superpixel-based graph representations are constructed in which each node represents a homogeneous image region and edges represent spectral-spatial similarity relationships among the formed regions.Graph Attention Networks (GATs) are then employed to adaptively propagate information across connected nodes through attention mechanisms.

5.6 Validation and Accuracy Assessment

The validation and accuracy assessment of the proposed spectral unmixing framework were performed using reference abundance maps generated from the available shapefile data. Initially, the shapefile-derived regions were converted into fractional reference abundance maps . The consistency of these reference abundance maps were further examined using geometrical and statistical validation metrics such as the coefficient of determination (R^2).

Subsequently, the proposed unmixing model was used to generate predicted fractional abundance maps for each endmember. The predicted abundances were then quantitatively compared against the reference abundance maps in order to evaluate reconstruction accuracy and spectral consistency. For this purpose, Root Mean Square Error (RMSE) and Average Absolute Difference (AAD) metrics were computed between the predicted and reference abundance values.

5.6.1 Accuracy Assessment Metrics for each proposed method

The performance of the spectral unmixing model was evaluated by comparing the predicted abundance maps with the reference abundance maps derived from the polygon-overlap methodology. Two quantitative metrics were employed: Root Mean

Square Error (RMSE) and Average Absolute Difference (AAD).

Let $A_c(i,j)$ denote the reference abundance of class c at pixel (i,j), and $\hat{A}_c(i,j)$ denote the corresponding predicted abundance. Let N represent the total number of pixels in the image.

5.7 Accuracy Assessment Metrics

The performance of the abundance estimation framework was evaluated using Root Mean Square Error (RMSE) and Average Absolute Difference (AAD). These metrics quantify the discrepancy between the reference abundance maps and the predicted abundance maps generated by the proposed model.

Let $A_c(i)$ denote the reference abundance of class c at pixel i, and let $\hat{A}_c(i)$ denote the corresponding predicted abundance. Furthermore, let N represent the total number of pixels and C denote the total number of abundance classes.

5.7.1 Root Mean Square Error (RMSE)

Class-wise RMSE

Class-wise RMSE measures the average magnitude of the prediction error for a particular abundance class while assigning greater weight to larger deviations. It is defined as

$$\mathrm{RMSE}_c = \sqrt{\frac{1}{N}\sum_{i=1}^{N}\Big(A_c(i) - \hat{A}_c(i)\Big)^2}.$$

A lower RMSE value indicates closer agreement between the predicted and reference abundance maps for class c.

Global RMSE

While class-wise RMSE evaluates the estimation accuracy of an individual abundance class, Global RMSE provides a single measure of the overall abundance estimation performance across all classes and pixels. It is computed as

$$\mathrm{RMSE}_{\mathrm{Global}} = \sqrt{\frac{1}{NC}\sum_{c=1}^{C}\sum_{i=1}^{N}\Big(A_c(i) - \hat{A}_c(i)\Big)^2}.$$

A lower Global RMSE value indicates better overall agreement between the predicted and reference abundance maps across the entire scene.

5.7.2 Average Absolute Difference (AAD)

Class-wise AAD

AAD quantifies the average absolute deviation between the predicted and reference abundances for a particular class and is defined as

$$\mathrm{AAD}_c = \frac{1}{N} \sum_{i=1}^{N} \left| A_c(i) - \hat{A}_c(i) \right|.$$

Unlike RMSE, AAD treats all prediction errors linearly and is therefore less sensitive to large outliers.

Global AAD

Global AAD measures the average absolute deviation across all abundance classes and pixels and is computed as

$$\mathrm{AAD}_{\mathrm{Global}} = \frac{1}{NC} \sum_{c=1}^{C} \sum_{i=1}^{N} \left| A_c(i) - \hat{A}_c(i) \right|.$$

A lower Global AAD value indicates improved overall abundance estimation performance across the entire image.

5.7.3 Endmember-Abundance Map Correspondence

The abundance estimation methods employed in this study generate multiple abundance maps corresponding to the extracted endmembers. For each unmixing method, namely Autoencoder-Based Spectral Unmixing, and Hybrid CNN-GAT Spectral Unmixing, every predicted abundance map was compared against each reference abundance map. The Root Mean Square Error (RMSE) and Average Absolute Difference (AAD) were computed for all possible pairings.The predicted abundance map exhibiting the lowest error with respect to a particular reference class was assigned to that endmember. This procedure was repeated until a one-to-one correspondence between all predicted abundance maps and reference endmember classes was obtained.

5.8 Workflow Summary

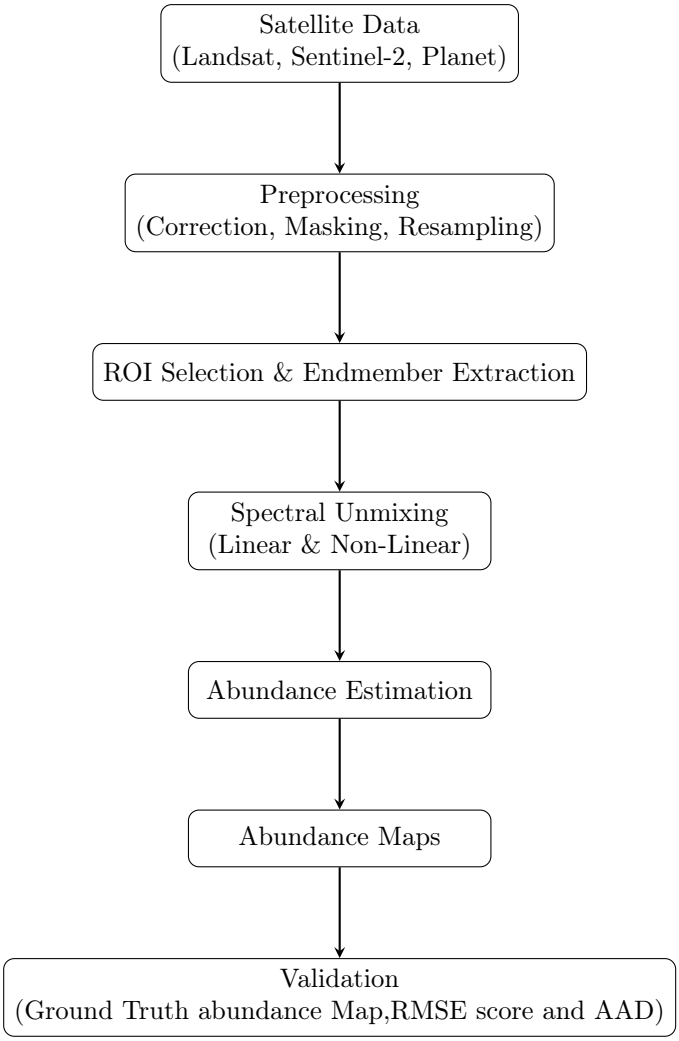

Figure 5.1: Compact methodology for spectral unmixing and validation

Chapter 6

Linear Spectral Unmixing

6.1 Simple Linear Spectral Unmixing

Let $\mathbf{x} \in \mathbb{R}^L$ denote the observed spectral vector of a pixel with L spectral bands. Assume that each pixel is a mixture of three materials (end members), whose spectral signatures are collected in the matrix

$$\mathbf{M} = [\mathbf{m}_1, \mathbf{m}_2, \mathbf{m}_3] \in \mathbb{R}^{L \times 3},$$

where $\mathbf{m}_k \in \mathbb{R}^L$ represents the spectral signature of the k-th endmember.

Let

$$\mathbf{f} = [f_1, f_2, f_3]^\top \in \mathbb{R}^3$$

be the abundance vector, where f_k denotes the fractional contribution of the k-th endmember.

The linear mixing model is

$$\mathbf{x} = \mathbf{M}\mathbf{f} + \boldsymbol{\varepsilon}, \qquad \boldsymbol{\varepsilon} \sim \mathcal{N}(\mathbf{0}, \sigma^2 \mathbf{I}).$$

Physically meaningful abundances satisfy

$$f_k \geq 0, \quad k = 1, 2, 3, \qquad \sum_{k=1}^{3} f_k = 1.$$

The main intuition here is that a end member can be present in a pixel or absent in the pixel but it can not contribute negatively in spectra . So every fraction of each end member must be greater than zero and the sum of all of them should be unity.

Under the Gaussian noise assumption, abundance estimation reduces to the con-

strained least-squares problem

$$\hat{\mathbf{f}} = \arg\min_{\mathbf{f}\in\mathbb{R}^3} \|\mathbf{x} - \mathbf{M}\mathbf{f}\|_2^2 \quad \text{s.t.} \quad \mathbf{f} \succeq \mathbf{0},\ \mathbf{1}^\top \mathbf{f} = 1.$$

For an image with N pixels,

$$\mathbf{X} = [\mathbf{x}_1, \ldots, \mathbf{x}_N] \in \mathbb{R}^{L\times N},$$

the global model is

$$\mathbf{X} = \mathbf{M}\mathbf{F} + \mathbf{E}, \qquad \mathbf{E} \sim \mathcal{N}(\mathbf{0}, \sigma^2\mathbf{I}),$$

where $\mathbf{F} \in \mathbb{R}^{3\times N}$ contains all abundance vectors.

6.2 Solution of the Linear Unmixing Optimization Problem

The unconstrained least-squares solution is

$$\mathbf{f}_{\text{LS}} = (\mathbf{M}^\top\mathbf{M})^{-1}\mathbf{M}^\top\mathbf{x},$$

which generally violates the physical constraints.

Introducing Lagrange multipliers yields the KKT conditions

$$\mathbf{M}^\top\mathbf{M}\mathbf{f} - \mathbf{M}^\top\mathbf{x} + \frac{\lambda}{2}\mathbf{1} - \frac{1}{2}\boldsymbol{\mu} = \mathbf{0},$$

$$\mathbf{1}^\top\mathbf{f} = 1, \quad \mathbf{f} \succeq \mathbf{0}, \quad \boldsymbol{\mu} \succeq \mathbf{0}, \quad \mu_k f_k = 0.$$

This yields the *Fully Constrained Least Squares* (FCLS) solution.The new constraints we introduce so that we can get the two conditions of having each fractional abundance greater than zero and the sum of all fractional abundance summing into unity satisfied.

To get the least square solution or more precisely fully constrained least square solution we must have the endmember matrix M.Now we describe the method for calculation of end member matrix M.

Computation of the Endmember Matrix M. If the ROI for endmember j contains N_j pixels(as we were supplied with shapefiles of each end member so from that geometry we know how many pixels fall into a particular class) $\{\mathbf{x}_1, \ldots, \mathbf{x}_{N_j}\}$, then

$$\mathcal{C}_j = \frac{1}{N_j}\sum_{i=1}^{N_j} \mathbf{x}_i.$$

The endmember matrix is

$$\mathbf{M} = [\mathcal{C}_1\ \mathcal{C}_2\ \mathcal{C}_3].$$

The individual spectra of each end member of LandSat data is plotted as followed:

Average Endmember Reflectance Values

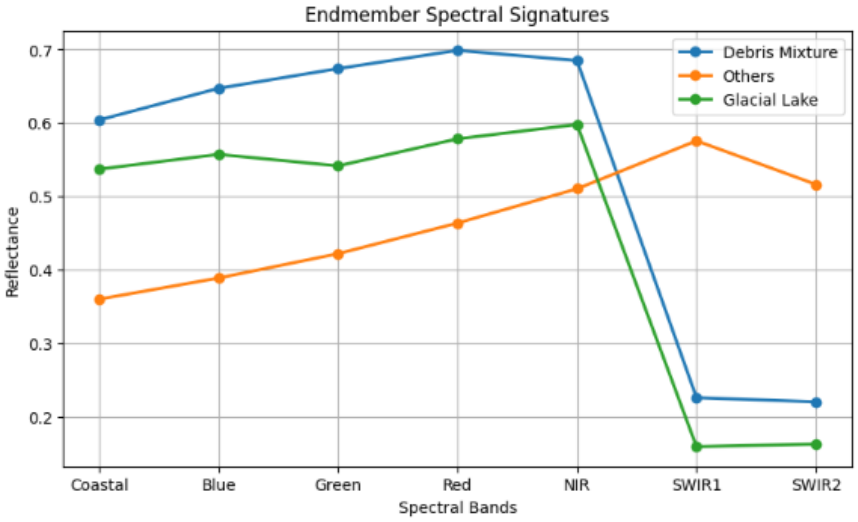

Figure 6.1: Average endmember reflectance values obtained from the shapefile-based spectral extraction process. The plot represents the spectral response of the selected constituent classes across different Landsat bands.

It can be seen evidently that the end member spectral reflectance curve plots are clearly separated from each other hence linear spectral unmixing approach can be applied here . Now in the below section a description is given about predicted and actual dataset size and the results obtained after performing simple linear spectral unmixing. [1] [2]

6.3 Dataset Statistics

Table 6.1: Dataset Statistics

Parameter	**Value**
Ground Truth Shape	(3, 1217, 2811)
Prediction Shape	(3, 1217, 2811)

6.4 Overall Performance under Simple Linear Spectral Unmixing approach

6.5 Overall Quantitative Metrics

The abundance reconstruction performance was quantitatively evaluated using Root Mean Square Error (RMSE) and Average Absolute Difference (AAD).

Table 6.2: Overall evaluation metrics

Metric	**Value**
RMSE	0.6454696
AAD	0.48604795

Source: Computed from abundance reconstruction outputs.

6.6 Per-Class Performance

Table 6.3 summarizes the class-wise quantitative evaluation metrics for the three endmember classes.

Table 6.3: Per-class evaluation metrics

Class	**RMSE**	**AAD**
Debris	0.795319	0.734170
Others	0.651428	0.523969
Glacial Lake	0.439320	0.200005

Source: Computed from abundance reconstruction outputs.

6.7 Mahalanobis Spectral Unmixing

Motivation

If noise has covariance $\mathbf{S}$ that is not a scalar multiple of the identity, the Euclidean least-squares criterion leads to suboptimal solution. The Mahalanobis distance

$$(\mathbf{y} - \mathbf{Mf})^\top \mathbf{S}^{-1} (\mathbf{y} - \mathbf{Mf})$$

accounts for correlation coefficeints and unequal variances accross the spectral bands.

BLUE Property of the Mahalanobis Estimator

The Mahalanobis-distance-based estimator corresponds to the Generalized Least Squares (GLS) estimator and is a Best Linear Unbiased Estimator (BLUE) under correlated noise conditions.

Consider the linear spectral mixing model

$$\mathbf{y} = \mathbf{M}\mathbf{f} + \boldsymbol{\varepsilon}, \qquad E(\boldsymbol{\varepsilon}) = 0, \qquad \mathrm{Cov}(\boldsymbol{\varepsilon}) = \mathbf{S}.$$

The GLS estimator is obtained by minimizing the Mahalanobis distance

$$\hat{\mathbf{f}}_{\mathrm{GLS}} = \arg\min_{\mathbf{f}} (\mathbf{y} - \mathbf{M}\mathbf{f})^{\top} \mathbf{S}^{-1} (\mathbf{y} - \mathbf{M}\mathbf{f}).$$

The resulting estimator is

$$\hat{\mathbf{f}}_{\mathrm{GLS}} = (\mathbf{M}^{\top}\mathbf{S}^{-1}\mathbf{M})^{-1}\mathbf{M}^{\top}\mathbf{S}^{-1}\mathbf{y}.$$

Linearity Define

$$\mathbf{A} = (\mathbf{M}^{\top}\mathbf{S}^{-1}\mathbf{M})^{-1}\mathbf{M}^{\top}\mathbf{S}^{-1}.$$

Then,

$$\hat{\mathbf{f}}_{\mathrm{GLS}} = \mathbf{A}\mathbf{y}.$$

Hence, the estimator is linear in the observed spectral vector $\mathbf{y}$.

Unbiasedness Taking expectation,

$$E(\hat{\mathbf{f}}_{\mathrm{GLS}}) = \mathbf{A}E(\mathbf{y}).$$

Since

$$E(\mathbf{y}) = \mathbf{M}\mathbf{f},$$

we obtain

$$E(\hat{\mathbf{f}}_{\mathrm{GLS}}) = (\mathbf{M}^{\top}\mathbf{S}^{-1}\mathbf{M})^{-1}\mathbf{M}^{\top}\mathbf{S}^{-1}\mathbf{M}\mathbf{f}.$$

Using

$$(\mathbf{M}^{\top}\mathbf{S}^{-1}\mathbf{M})^{-1}(\mathbf{M}^{\top}\mathbf{S}^{-1}\mathbf{M}) = \mathbf{I},$$

therefore,

$$E(\hat{\mathbf{f}}_{\text{GLS}}) = \mathbf{f}.$$

Hence, the estimator is unbiased.

Covariance of the Estimator The covariance of the estimator is

$$\text{Cov}(\hat{\mathbf{f}}_{\text{GLS}}) = \mathbf{A}\,\text{Cov}(\mathbf{y})\,\mathbf{A}^{\top}.$$

Since

$$\text{Cov}(\mathbf{y}) = \mathbf{S},$$

we get

$$\text{Cov}(\hat{\mathbf{f}}_{\text{GLS}}) = (\mathbf{M}^{\top}\mathbf{S}^{-1}\mathbf{M})^{-1}.$$

Minimum Variance Property Consider another arbitrary linear unbiased estimator

$$\tilde{\mathbf{f}} = \mathbf{C}\mathbf{y},$$

satisfying

$$\mathbf{C}\mathbf{M} = \mathbf{I}.$$

Define

$$\mathbf{D} = \mathbf{C} - \mathbf{A}.$$

Then,

$$\mathbf{D}\mathbf{M} = 0.$$

The covariance difference becomes

$$\text{Cov}(\tilde{\mathbf{f}}) - \text{Cov}(\hat{\mathbf{f}}_{\text{GLS}}) = \mathbf{D}\mathbf{S}\mathbf{D}^{\top}.$$

Since the covariance matrix $\mathbf{S}$ is positive definite,

$$\mathbf{D}\mathbf{S}\mathbf{D}^{\top} \geq 0.$$

Therefore,

$$\mathrm{Cov}(\tilde{\mathbf{f}}) \geq \mathrm{Cov}(\hat{\mathbf{f}}_{\mathrm{GLS}}).$$

Thus, no other linear unbiased estimator possesses lower covariance than the Mahalanobis-distance-based GLS estimator.

Hence, the Mahalanobis estimator is a

Best Linear Unbiased Estimator (BLUE)

for spectral unmixing under correlated noise assumptions.

Model and Estimator

Assume

$$\mathbf{y} = \mathbf{M}\mathbf{f} + \boldsymbol{\varepsilon}, \qquad \mathrm{Cov}(\boldsymbol{\varepsilon}) = \mathbf{S},$$

where $\mathbf{M} \in \mathbb{R}^{p\times 3}$.

The GLS estimator is

$$\hat{\mathbf{f}}_{\mathrm{GLS}} = (\mathbf{M}^\top \mathbf{S}^{-1}\mathbf{M})^{-1}\mathbf{M}^\top \mathbf{S}^{-1}\mathbf{y}.$$

Covariance Estimation

For each endmember j,

$$\mathbf{S}_j = \frac{1}{N_j - 1}\sum_{i=1}^{N_j}(\mathbf{x}_i - \boldsymbol{\mu}_j)(\mathbf{x}_i - \boldsymbol{\mu}_j)^\top.$$

The average covariance is

$$\mathbf{S} = \frac{1}{3}\sum_{j=1}^{3}\mathbf{S}_j.$$

Transformation to Implement the GLS Estimator

Observe that the estimator

$$\hat{\mathbf{f}}_{\mathrm{GLS}}$$

can be obtained by defining the transformed variables

$$\tilde{\mathbf{y}} = \mathbf{S}^{-1/2}\mathbf{y}, \qquad \tilde{\mathbf{M}} = \mathbf{S}^{-1/2}\mathbf{M}.$$

as above and then The problem reduces to

$$\mathbf{f} = \arg\min_{\mathbf{f}} \|\tilde{\mathbf{y}} - \tilde{\mathbf{M}}\mathbf{f}\|_2^2.$$

The obtained objective abundance of Linear Spectral Unmixing approach does not satisfy the required physical constraint .

NNLS with Sum-to-One Constraint

The abundances must be greater than zero is taken care of by taking into consideration of the non negative least square subroutine use

$$\mathbf{f} = \text{NNLS}(\tilde{\mathbf{M}}, \tilde{\mathbf{y}}),$$

After getting satisfied the non negativity constraint each one of the fractional abundance was normalized to satisfy sum to unity constraint.

$$\mathbf{f} \leftarrow \frac{\mathbf{f}}{\sum_{j=1}^{3} f_j}.$$

This ensures non-negativity and sum-to-one constraints. [1] [2]

6.8 Evaluation of Mahalanobis Spectral Unmixing Results

6.8.1 Dataset Statistics

Table 6.4: Dataset statistics used for Mahalanobis spectral unmixing evaluation

Parameter	Value
Ground truth shape	(3, 1217, 2811)
Prediction shape	(3, 1217, 2811)

Source: Computed from Mahalanobis spectral unmixing outputs.

6.8.2 Overall Quantitative Metrics

The abundance reconstruction accuracy was quantitatively evaluated using Root Mean Square Error (RMSE) and Average Absolute Difference (AAD).

Table 6.5: Overall quantitative metrics for Mahalanobis spectral unmixing

Metric	**Value**
RMSE	0.5421
AAD	0.3497

Source: Computed from Mahalanobis abundance reconstruction results.

6.8.3 Per-Class Performance

Table 6.6 summarizes the class-wise evaluation metrics obtained for the three end-members using Mahalanobis spectral unmixing.

Table 6.6: Per-class evaluation metrics for Mahalanobis spectral unmixing

Class	**RMSE**	**AAD**
Debris	0.6737	0.5094
Others	0.5286	0.3388
Glacial Lake	0.3852	0.2008

Source: Computed from Mahalanobis spectral unmixing outputs.

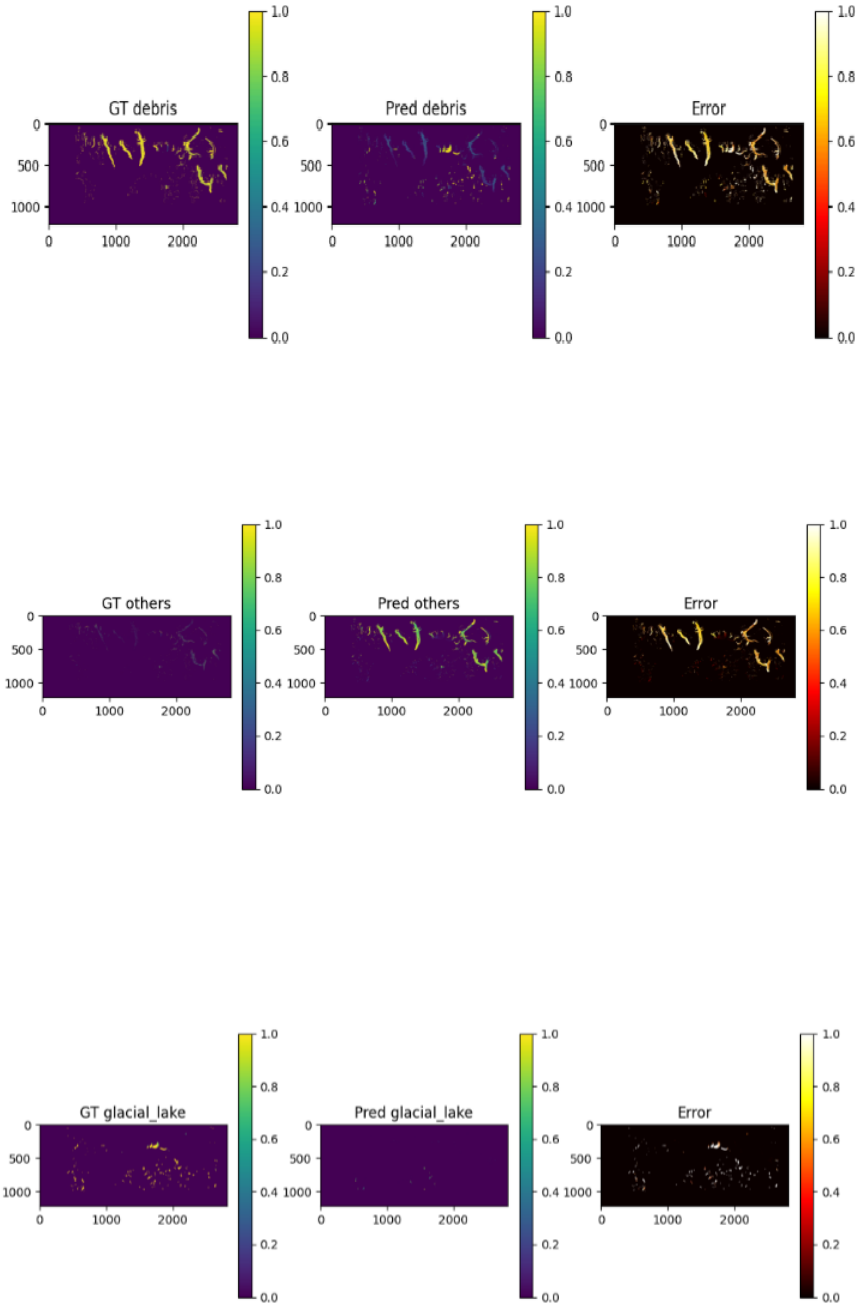

Figure 6.2: Error maps for different classes showing reconstruction differences between predicted and ground truth abundances by linear spectral unmixing approach.

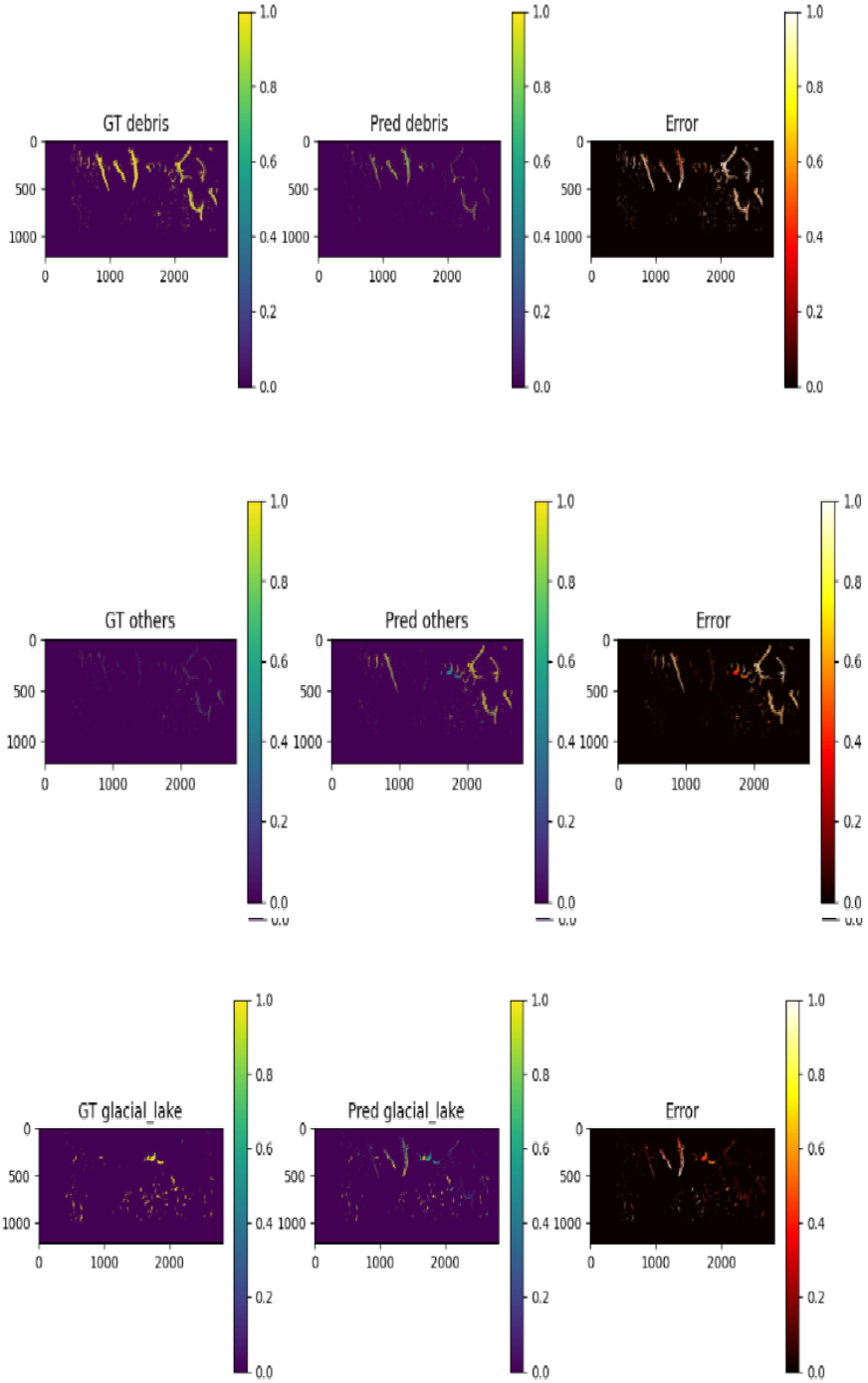

Figure 6.3: Error maps for different classes showing reconstruction differences between predicted and ground truth abundances under Mahalanobis Spectral Unmixing.

Chapter 7

Non Linear Spectral Unmixing using Autoencoder

7.0.1 Motivation for Using Autoencoder-Based Spectral Unmixing

Traditional linear spectral unmixing methods assume that the observed hyperspectral pixel is formed through a linear combination of end member spectra.In real-world scenarios, spectral interactions are often nonlinear due to multiple scattering effects, atmospheric influence, sensor noise.

Conventional deep neural networks are capable of learning nonlinear mappings, they generally focus only on predicting abundance values and do not explicitly enforce spectral reconstruction consistency. In spectral unmixing, it is important to estimate accurate abundance maps but it is also required to ensure that the reconstructed spectra remain very close to the original observed spectra. This reconstruction constraint preserves the physical meaning of the unmixing process.

Autoencoder-based architectures are therefore more suitable for spectral unmixing because they naturally incorporate both objectives simultaneously. The encoder learns a compact latent representation corresponding to fractional abundances, while the decoder reconstructs the original spectra from these estimated abundances. Consequently, the model is trained under two important constraints:

- The reconstructed spectra should be as close as possible to the original input spectra.
- The generated fractional abundance maps should closely approximate the true abundance distributions.

This dual optimization framework allows autoencoders to model nonlinear spectral mixtures more effectively while maintaining reconstruction fidelity and physical interpretability.

7.1 Autoencoder based specteral unmixing

Classical linear spectral unmixing assumes that each observed pixel spectrum $x \in \mathbb{R}^B$ is a convex combination of K endmember spectra:

$$x = \sum_{k=1}^{K} a_k e_k + \epsilon, \qquad a_k \geq 0, \qquad \sum_{k=1}^{K} a_k = 1, \tag{7.1}$$

where e_k denotes the k-th endmember, a_k is its fractional abundance, and ϵ represents noise and modeling error.

The proposed autoencoder learns the same structure *implicitly*.

Encoder as Abundance Estimator

The encoder maps each pixel spectrum x to a latent vector

$$a = f_\theta(x) \in \mathbb{R}^K. \tag{7.2}$$

The final *Softmax* layer enforces

$$a_k \geq 0, \qquad \sum_{k=1}^{K} a_k = 1, \tag{7.3}$$

which exactly matches the physical constraints of abundance fractions in spectral unmixing.

Decoder as Learned Mixing Model

The decoder reconstructs the spectrum as

$$\hat{x} = g_\phi(a), \tag{7.4}$$

and therefore plays the role of a *nonlinear mixing function*. Unlike classical linear unmixing, this formulation can model:

- multiple scattering effects,
- sub-pixel material interactions,
- illumination and atmospheric variations.

Training Objective as Physical Consistency

The network is trained by minimizing the reconstruction error:

$$\mathcal{L} = \|x - \hat{x}\|_2^2 + 0.5 \left(1 - \frac{x^\top \hat{x}}{\|x\|_2 \|\hat{x}\|_2}\right) \tag{7.5}$$

which forces the model to explain each observed spectrum solely through its abundance vector. The latent representation therefore becomes the only physically meaningful explanation of the pixel.

ROI-Guided Semantic Alignment

Because the training samples are drawn from pure or near-pure region-of-interest (ROI) polygons, the encoder learns a latent basis aligned with real endmembers. Each latent dimension becomes semantically meaningful:

$$a = \left[a_{\text{debris}}, a_{\text{others}}, a_{\text{glacial lake}}\right]. \tag{7.6}$$

As a result, the autoencoder is not merely a dimensionality reduction model, but a physics-aware nonlinear unmixing framework that respects abundance constraints, learns complex mixing behavior, and produces interpretable fractional abundance maps across the entire scene.

7.2 Autoencoder Architecture

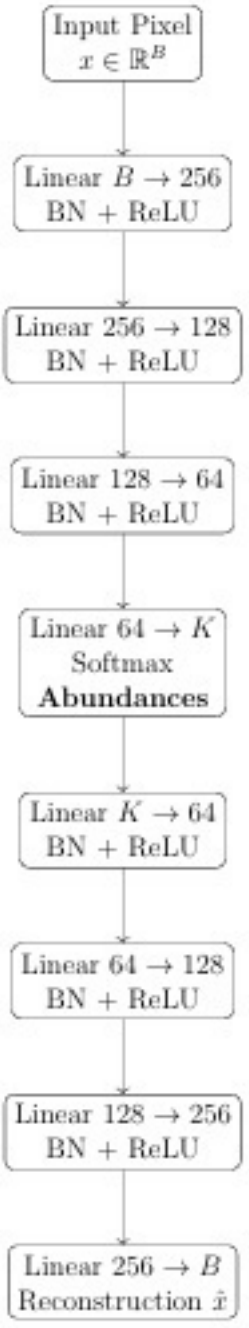

Figure 7.1: Architectural flow of the Autoencoder-based spectral unmixing framework.

7.2.1 Evaluation of Nonlinear Spectral Unmixing Results

Dataset Statistics

Table 7.1: Dataset statistics used for quantitative evaluation

Parameter	Value
Ground truth shape	(3, 1217, 2811)
Prediction shape	(3, 1217, 2811)

Source: Computed from abundance reconstruction outputs.

Overall Quantitative Metrics

Table 7.2: Overall quantitative evaluation metrics

Metric	Value
RMSE	0.111515
AAD	0.020265

Per-Class Performance Evaluation

The class-wise quantitative evaluation results for the three endmembers are summarized in Table 7.3.

Table 7.3: Per-class evaluation metrics for the three endmembers

Class	RMSE	AAD
Debris	0.148513	0.030337
Others	0.092919	0.016831
Glacial Lake	0.081342	0.013625

Source: Computed from abundance reconstruction outputs.

Visual Comparison of Abundance Maps

Figures 7.2, 7.3, and 7.4 present the visual comparison between the ground truth abundance maps, predicted abundance maps.

The comparison demonstrates that the proposed framework successfully reconstructs the spatial abundance distribution patterns .

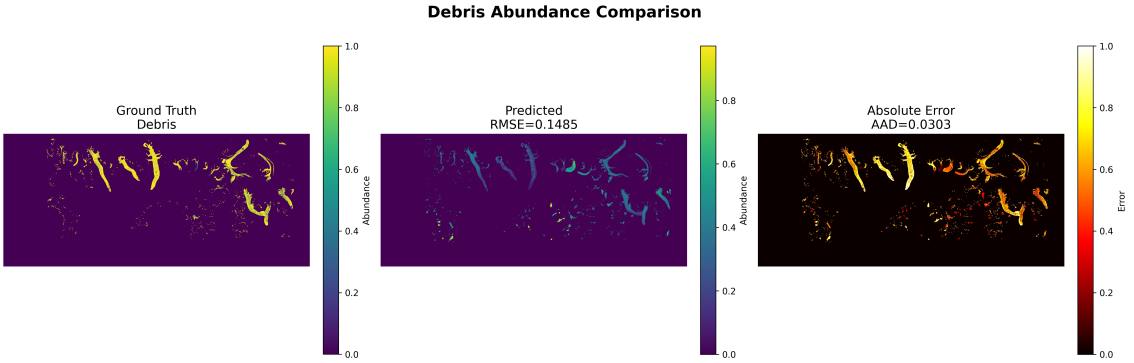

Figure 7.2: Comparison of ground truth abundance map, predicted abundance map, and absolute error map for the Debris class.

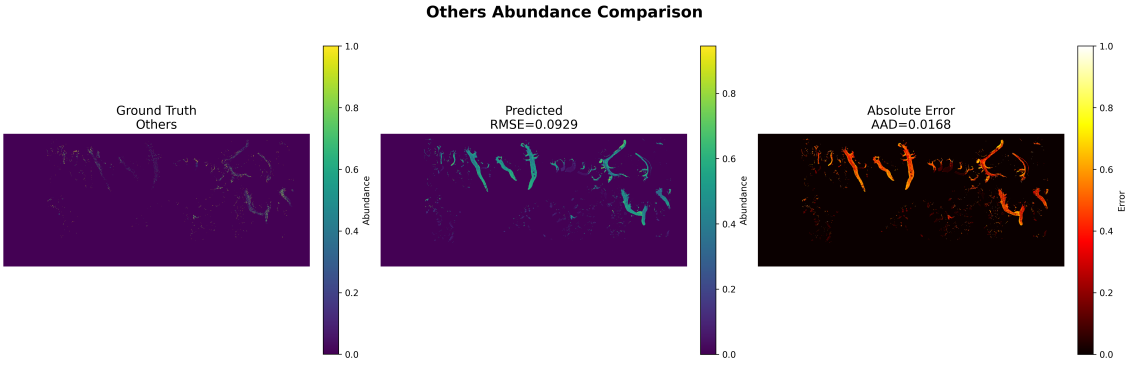

Figure 7.3: Comparison of ground truth abundance map, predicted abundance map, and absolute error map for the Others class.

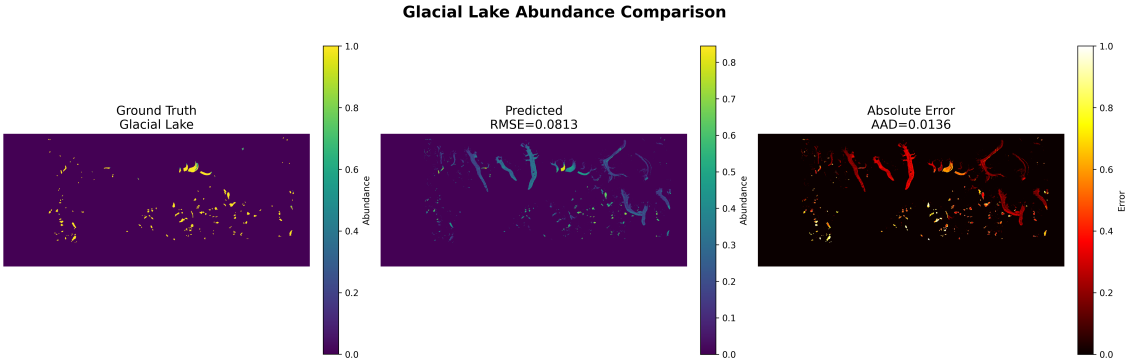

Figure 7.4: Comparison of ground truth abundance map, predicted abundance map, and absolute error map for the Glacial Lake class.

Chapter 8

Graph Neural Network Based Spectral Unmixing

8.1 Motivation for Graph-Based Modeling

Traditional spectral unmixing approaches generally treat each pixel independently. However, in real-world hyperspectral and multispectral imagery, neighboring pixels often exhibit strong spatial as well as spectral correlations. Therefore, the independence assumption becomes inadequate for modeling complex land-cover interactions.

To address this limitation, graph-based representations can be utilized. In a graph formulation, nodes represent image regions or superpixels, while edges capture relationships among neighboring regions based on spectral and spatial similarity. Such a representation enables the application of Graph Neural Networks (GNNs), which facilitate modeling of long-range dependencies and contextual relationships effectively.

The proposed Hybrid CNN-GAT framework combines the local feature extraction capability of Convolutional Neural Networks (CNNs) with the global relational modeling capability of Graph Attention Networks (GATs). This allows the model to learn both spectral and spatial dependencies jointly.

8.2 Proposed Methodology

8.2.1 Graph Construction

The input multispectral image (7 bands) is first transformed into a lower-dimensional feature representation using Principal Component Analysis (PCA) to obtain three bands. The reduced feature map is then segmented into superpixels using the SLIC segmentation algorithm.

Each superpixel is considered a graph node. Spatial and spectral similarities

among superpixels are used to construct graph edges using K-Nearest Neighbor (KNN) connectivity.

The edge weight between nodes is computed as:

$$w_{ij} = \exp\left(-\frac{d_{ij}^2}{\sigma^2}\right)$$

where d_{ij} represents the distance between nodes i and j.

Initially, convolutional layers of the model extract local spectral-spatial representations from the image. These features are aggregated over superpixels and passed through graph attention layers to capture global contextual information.

The fused features are then used to estimate abundance vectors satisfying abundance constraints. [3]

8.3 Algorithms

8.3.1 SLIC Superpixel Segmentation Algorithm

Algorithm 1 SLIC Superpixel Segmentation

Require: Feature map $\mathbf{Z} \in \mathbb{R}^{H \times W \times d}$, number of segments K, compactness parameter m

Ensure: Segmentation map $S(i, j)$

Initialize cluster centers on a regular grid
Compute spacing:
$S = \sqrt{\frac{HW}{K}}$
for each pixel i **do**
    $\mathbf{p}_i = [\mathbf{z}_i, x_i, y_i]$
end for
repeat
    for each cluster center k **do**
        for pixels in the $2S \times 2S$ neighborhood **do**
            Compute distance:
            $D(i,k) = \sqrt{\left(\frac{\|\mathbf{z}_i - \mathbf{z}_k\|}{m}\right)^2 + \left(\frac{\|(x_i,y_i)-(x_k,y_k)\|}{S}\right)^2}$
            Assign nearest cluster:
            $S(i,j) = \arg\min_k D(i,k)$
        end for
    end for
    for each cluster k **do**
        Update cluster center:
        $\mathbf{c}_k = \frac{1}{|\mathcal{S}_k|} \sum_{i \in \mathcal{S}_k} \mathbf{p}_i$
    end for
until convergence
return $S(i, j)$

8.3.2 Graph Construction Algorithm

Algorithm 2 Graph Construction using PCA, SLIC and KNN

Require: Hyperspectral image $\mathbf{I} \in \mathbb{R}^{B \times H \times W}$

Ensure: Graph $G = (V, E, W)$

Reshape image into spectral matrix:

$\mathbf{X} \in \mathbb{R}^{(HW) \times B}$

Apply PCA for dimensionality reduction:

$\mathbf{Z} = \mathbf{X}\mathbf{W}$

Perform SLIC superpixel segmentation on $\mathbf{Z}$

for each superpixel segment k **do**

    Compute node spectral feature:

    $\mathbf{x}_k = \frac{1}{|\mathcal{S}_k|} \sum \mathbf{I}_{:,i,j}$

    Compute spatial centroid:

    $\mathbf{c}_k = \frac{1}{|\mathcal{S}_k|} \sum (i, j)$

end for

Construct spectral KNN graph

Construct spatial KNN graph

Compute edge weights:

$w_{ij} = \exp\left(-\frac{d_{ij}^2}{\sigma^2}\right)$

return Graph $G = (V, E, W)$

8.3.3 Hybrid CNN-GAT Spectral Unmixing Algorithm

Algorithm 3 Hybrid CNN-GAT Spectral Unmixing

Require: Image $\mathbf{I}$, graph G, endmember matrix $\mathbf{M}$

Ensure: Reconstructed spectra $\hat{\mathbf{Y}}$, abundances $\mathbf{A}$

Spectral reduction:

$\mathbf{F}_{local} = \sigma\left(W_2 * \sigma(W_1 * \mathbf{I})\right)$

CNN feature extraction:

$\mathbf{F}_{cnn} = \sigma\left(W_4 * \sigma(W_3 * \mathbf{F}_{local})\right)$

Superpixel aggregation:

$\mathbf{f}_k = \frac{1}{|\mathcal{S}_k|} \sum \mathbf{F}_{cnn}(i,j)$

Graph attention propagation:

$\mathbf{h}_i = \sum_{j \in \mathcal{N}(i)} \alpha_{ij} W \mathbf{f}_j$

Feature fusion:

$\mathbf{F}_{fused} = [\mathbf{F}^{sp}_{local} \,||\, \mathbf{F}_{global}]$

Abundance estimation:

$\mathbf{A} = \text{softmax}\left(MLP(\mathbf{F}_{fused})\right)$

Reconstruction:

$\hat{\mathbf{Y}} = \mathbf{AM}$

return $\hat{\mathbf{Y}}, \mathbf{A}$

8.4 Model Architecture Overview

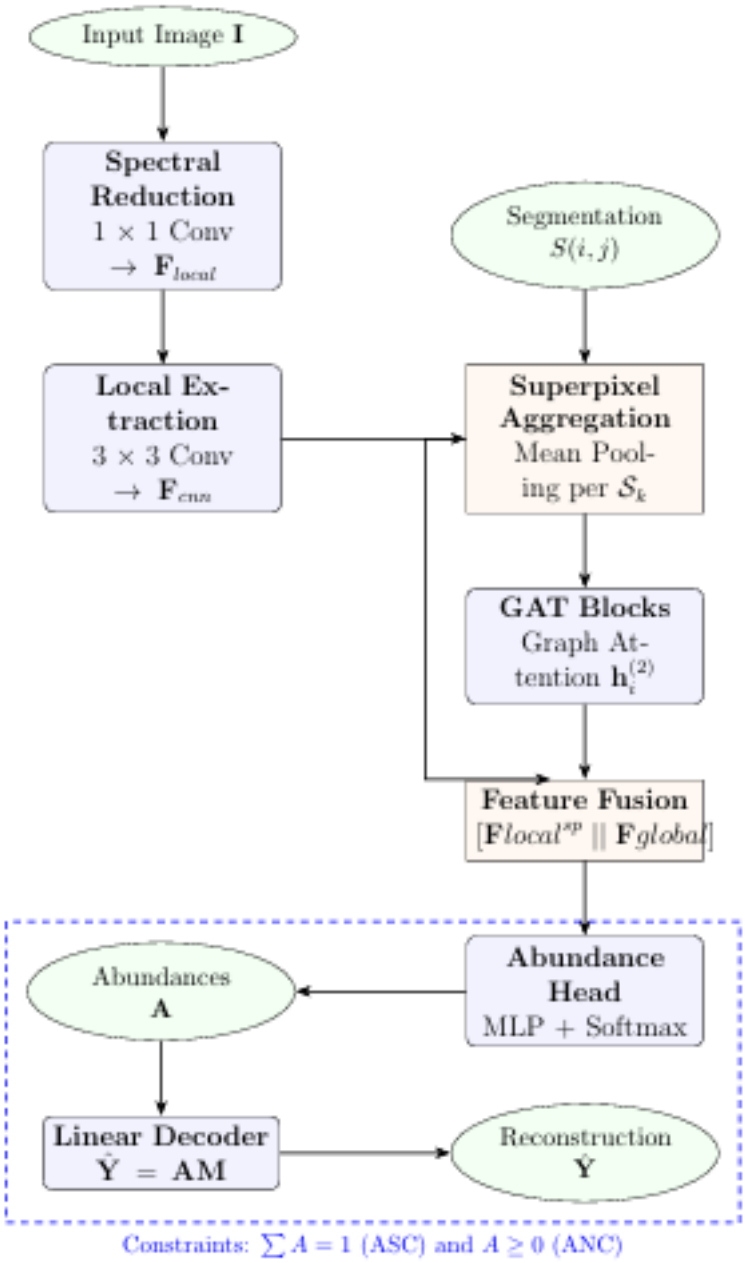

Figure 8.1: Architectural flow of the proposed Hybrid CNN-GAT spectral unmixing framework integrating CNN-based local feature extraction with GAT-based global contextual modeling.

8.5 Results and Evaluation

8.5.1 Overall Performance

The overall abundance reconstruction performance of the proposed framework was evaluated using Root Mean Square Error (RMSE) and Average Absolute Difference

(AAD).

Table 8.1: Overall evaluation metrics

Metric	**Value**
RMSE	0.3671
AAD	0.3228

Source: Computed from abundance reconstruction outputs.

8.5.2 Per-Class Performance

Table 8.2 summarizes the class-wise quantitative evaluation metrics obtained for the three endmember classes.

Table 8.2: Per-class evaluation metrics

Class	**RMSE**	**AAD**
Debris	0.4317	0.4004
Others	0.3067	0.2795
Glacial Lake	0.3520	0.2886

Source: Computed from multispectral abundance reconstruction outputs.

8.5.3 Error Map Analysis

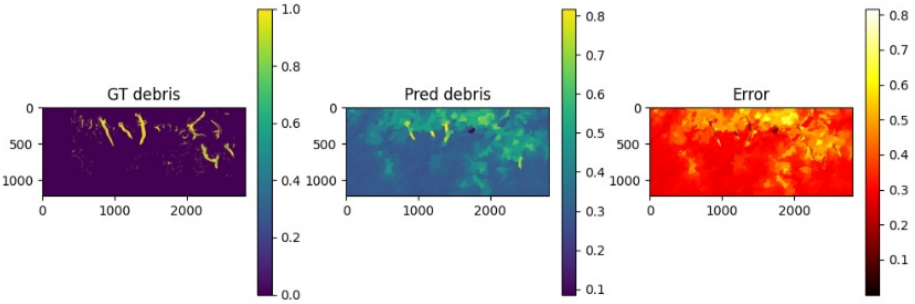

(a) Error Map (Debris)

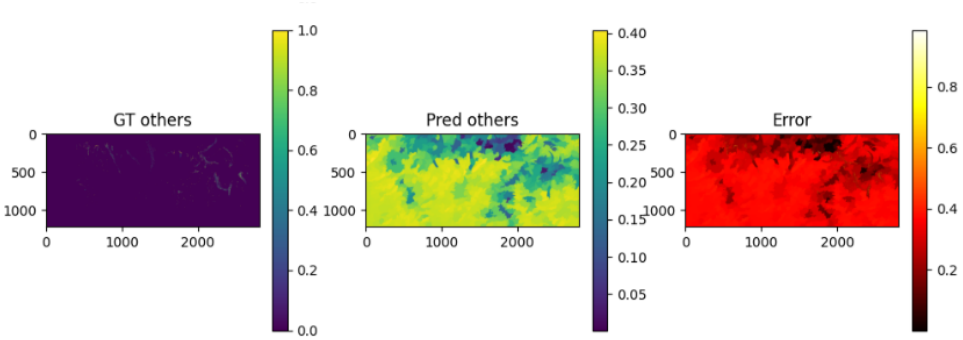

(b) Error Map (Others)

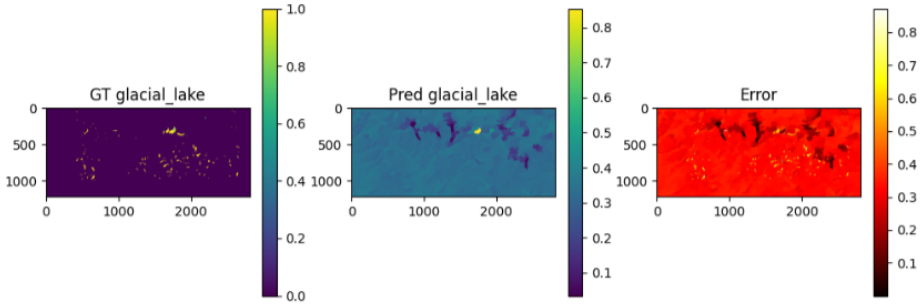

(c) Error Map (Glacial Lake)

Figure 8.2: Error maps showing reconstruction differences between predicted and ground-truth abundance values using Graph Neural Networks.

8.5.4 Training Convergence Analysis

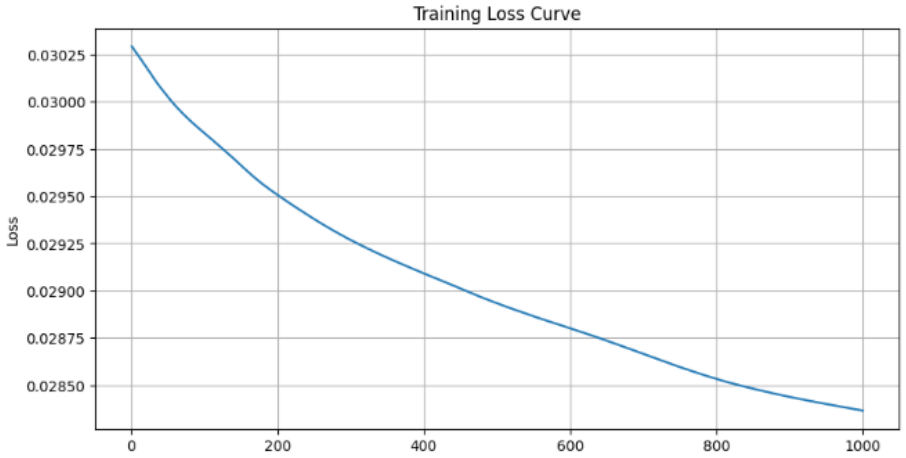

Figure 8.3: Training loss curve of the proposed CNN-GAT model over 1000 epochs. The gradual decrease in loss indicates stable convergence during training.

8.6 Discussion

Overall, the integration of CNN-based local feature extraction with GAT-based global contextual modeling yields higher reconstruction errors than traditional autoencoder-based models. Some of the underlying reasons for this phenomenon include:

1. **Representation Learning:**

   Graph Neural Networks propagate information through neighboring nodes, which risks distorting distinct spectral properties. Conversely, autoencoders directly capture latent characteristics through strict pixel-wise reconstruction, thereby the method preserves raw spectral individuality.

2. **Oversmoothing Effect:**

   Repeated graph convolutions inherently push neighboring node features toward uniformity .This reduces the discriminative spatial-spectral resolution of the model, whereas autoencoders preserve clearer spectral separability.

3. **Spatial Heterogeneity:**

   Spatial graph propagation may therefore introduce unwanted spectral cross-contamination across boundary features.

Chapter 9

Comparative Analysis of Spectral Unmixing Methods

9.1 Overall Quantitative Comparison

Table 9.1 summarizes the overall abundance estimation performance of all investigated methods.

Table 9.1: Overall comparison of spectral unmixing methods.

Method	RMSE	AAD
Linear Spectral Unmixing	0.6455	0.4860
Mahalanobis Spectral Unmixing	0.5421	0.3497
Autoencoder-Based Spectral Unmixing	0.1120	0.0200
Hybrid CNN-GAT Spectral Unmixing	0.3671	0.3228

Table 9.2: Per-class comparison of abundance estimation performance.

Method	Class	RMSE	AAD
Linear SU	Debris	0.7953	0.7342
	Others	0.6514	0.5240
	Glacial Lake	0.4393	0.2000
Mahalanobis SU	Debris	0.6737	0.5094
	Others	0.5286	0.3388
	Glacial Lake	0.3852	0.2008
Autoencoder	Debris	0.1490	0.0300
	Others	0.0930	0.0170
	Glacial Lake	0.0810	0.0140
CNN-GAT	Debris	0.4317	0.4004
	Others	0.3067	0.2795
	Glacial Lake	0.3520	0.2886

9.2 Overall Assessment

The comparative study demonstrates the following ranking based on abundance estimation accuracy:

1. Autoencoder-Based Spectral Unmixing
2. Hybrid CNN-GAT Spectral Unmixing
3. Mahalanobis Spectral Unmixing
4. Linear Spectral Unmixing

The Autoencoder achieved the best quantitative performance owing to its ability to model nonlinear spectral interactions while preserving abundance constraints.

The CNN-GAT framework introduces spatial-context modeling and graph-based information propagation, providing a more comprehensive spectral-spatial representation despite a slightly higher reconstruction error.

Chapter 10

Conclusion and Future Work

10.1 Conclusion

This dissertation presented a methodology for abundance estimation and glacier surface characterization using multi-spectral satellite imagery of a Himalayan glacier region.The proposed framework combined endmember extraction, spectral analysis, endmember aggregation, and autoencoder-based abundance estimation to derive fractional abundance maps. Experimental results demonstrates that the proposed approach successfully reconstructed the spectral information of the scene while producing spatially coherent abundance maps. Overall, the results indicate that the developed methodology is capable of producing reliable abundance estimates and offers a promising direction for remote sensing based glacier monitoring and climate-change assessment.

10.2 Future Work

The proposed frameworka demonstrate good performance for glacial lake abundance estimation but several research directions remain open for further investigation. Graph Transformers and hierarchical graph neural networks can be explored. Such architectures can further improve the accuracy and robustness of abundance estimation in glacial environment.Future work can extend the proposed framework to multi-temporal satellite observations climate-driven environmental changes over time.Finally, the computational efficiency can be improved through optimized graph construction strategies, GPU acceleration.

Bibliography

[1] A. E. Racoviteanu, L. Nicholson, and N. F. Glasser, "Surface composition of debris-covered glaciers across the himalaya using linear spectral unmixing of landsat 8 oli imagery," *The Cryosphere*, vol. 15, no. 9, pp. 4215–4237, 2021.

[2] C. Quintano, A. Fernandez-Manso, Y. E. Shimabukuro, and G. Pereira, "Spectral unmixing," *International Journal of Remote Sensing*, vol. 33, no. 18, pp. 5307–5326, 2012.

[3] H. Dong, X. Zhang, J. Zhang, H. Meng, and L. Jiao, "Graph-based adaptive network with spatial-spectral features for hyperspectral unmixing," *IEEE Journal of Selected Topics in Applied Earth Observations and Remote Sensing*, vol. 18, pp. 12865–12880, 2025.

[4] D. C. Heinz and C.-I. Chang, "Fully constrained least-squares linear spectral mixture analysis method for material quantification in hyperspectral imagery," *IEEE Transactions on Geoscience and Remote Sensing*, vol. 39, no. 3, pp. 529–545, 2001.

[5] J. M. Bioucas-Dias, A. Plaza, G. Camps-Valls, P. Scheunders, N. M. Nasrabadi, and J. Chanussot, "Hyperspectral unmixing overview: Geometrical, statistical, and sparse regression-based approaches," *IEEE Journal of Selected Topics in Applied Earth Observations and Remote Sensing*, vol. 5, no. 2, pp. 354–379, 2012.

[6] X. Liu, S. Bourennane, and C. Fossati, "Nonnegative matrix factorization with sparseness constraint for hyperspectral unmixing," *IEEE Transactions on Geoscience and Remote Sensing*, vol. 49, no. 11, pp. 4115–4127, 2011.

[7] R. A. Borsoi, T. Imbiriba, J. C. M. Bermudez, C. Richard, and P. Honeine, "Spectral variability in hyperspectral data unmixing: A comprehensive review," *IEEE Geoscience and Remote Sensing Magazine*, vol. 9, no. 4, pp. 223–270, 2021.

[8] T. Imbiriba, J. C. M. Bermudez, C. Richard, and P. Honeine, "Autoencoder-based hyperspectral unmixing," *IEEE Geoscience and Remote Sensing Letters*, vol. 16, no. 3, pp. 435–439, 2019.